



1 **Characterizing Uncertainties in Atmospheric Inversions of Fossil Fuel CO<sub>2</sub> Emissions in**  
2 **California**

3 Kieran Brophy<sup>1</sup>, Heather Graven<sup>1</sup>, Alistair J. Manning<sup>2</sup>, Emily White<sup>3</sup>, Tim Arnold<sup>4,5</sup>, Marc L  
4 Fischer<sup>6</sup>, Seongeun Jeong<sup>6</sup>, Xinguang Cui<sup>6</sup>, Matthew Rigby<sup>3</sup>

5

6 1. Department of Physics, Imperial College London, London, UK

7 2. Hadley Centre, Met Office, Exeter, UK

8 3. School of Chemistry, University of Bristol, Bristol, UK

9 4. National Physical Laboratory, London, UK

10 5. University of Edinburgh, Edinburgh, UK

11 6. Lawrence Berkeley National Laboratory, Berkeley, CA

12

13 Corresponding author:

14 Kieran Brophy

15 Email: [kb613@ic.ac.uk](mailto:kb613@ic.ac.uk)

16 **Key Words:** Fossil Fuel, Carbon Dioxide, Simulation Experiment, Inversion, Transport Error

17 **Abstract**

18 Atmospheric inverse modelling has become an increasingly useful tool for evaluating emissions  
19 of greenhouse gases including methane, nitrous oxide and synthetic gases such as  
20 hydrofluorocarbons (HFCs). Atmospheric inversions for emissions of CO<sub>2</sub> from fossil fuel  
21 combustion (ffCO<sub>2</sub>) are currently being developed. The aim of this paper is to investigate  
22 potential errors and uncertainties related to the spatial and temporal prior representation of  
23 emissions and modelled atmospheric transport for the inversion of ffCO<sub>2</sub> emissions in the U.S.  
24 state of California. We perform simulation experiments based on a network of ground-based  
25 observations of CO<sub>2</sub> concentration and radiocarbon in CO<sub>2</sub> (a tracer of ffCO<sub>2</sub>), combining prior  
26 (bottom-up) emission models and transport models currently used in many atmospheric studies.  
27 The potential effect of errors in the spatial and temporal distribution of prior emission estimates  
28 is investigated in experiments by using perturbed versions of the emissions estimates used to



29 create the pseudo data. The potential effect of transport error was investigated by using three  
30 different atmospheric transport models for the prior and pseudo data simulations. We find that  
31 the magnitude of biases in posterior state-total emissions arising from errors in the spatial and  
32 temporal distribution in prior emissions in these experiments are 1-15% of posterior state-total  
33 emissions, and generally smaller than the 2- $\sigma$  uncertainty in posterior emissions. Transport error  
34 in these experiments introduces biases of -10% to +6% in posterior state-total emissions. Our  
35 results indicate that uncertainties in posterior state-total ffCO<sub>2</sub> estimates arising from the choice  
36 of prior emissions or atmospheric transport model are on the order of 15% or less for the ground-  
37 based network in California we consider. We highlight the need for temporal variations to be  
38 included in prior emissions, and for continuing efforts to evaluate and improve the representation  
39 of atmospheric transport for regional ffCO<sub>2</sub> inversions.

## 40 **1. Introduction**

41 The U.S. state of California currently emits roughly 100 Tg C of fossil fuel CO<sub>2</sub> (ffCO<sub>2</sub>) each  
42 year (CARB, 2017), or approximately 1% of global emissions (Boden et al., 2016). The passing  
43 of California's "Global Warming Solutions Act" (AB-32) in 2006 requires that overall  
44 greenhouse gas emissions in California be reduced to their 1990 levels by 2020 (a 15% reduction  
45 compared to business as usual emissions) with further reductions of 40% below 1990 levels  
46 planned for 2030, and 80% below by 2050. The California Air Resources Board (CARB) is  
47 responsible for developing and maintaining a "bottom-up" inventory of greenhouse gas  
48 emissions to verify these reduction targets. However, previous studies have shown such  
49 inventories may have errors or incomplete knowledge of sources (e.g. Marland et al, 1999;  
50 Andres et al., 2012). Uncertainties in inventories of annual ffCO<sub>2</sub> emissions from most  
51 developed countries (i.e. UNFCCC Annex I and Annex II) have been estimated to be between 5-



52 10% (Andres et al., 2012), and uncertainties can become much larger at subnational levels  
53 (Hogue et al., 2016). In a recent study Fischer et al., (2017) found discrepancies between bottom-  
54 up gridded inventories of ffCO<sub>2</sub> emissions were 11% of California’s state total emissions.

55 Previous research has shown that inferring ffCO<sub>2</sub> emissions from atmospheric measurements,  
56 including measurements of ffCO<sub>2</sub> tracers, could provide independent emissions estimates on  
57 urban to continental scales (e.g. Basu et al., 2016; Fischer et al., 2017; Graven et al. 2018;  
58 INFLUX ref). Such estimates are derived from observations through the use of an atmospheric  
59 chemical transport model and a suitable inverse method in a process often referred to as “inverse  
60 modelling” or an “inversion”. Distinguishing enhancements of CO<sub>2</sub> due to anthropogenic or  
61 biogenic sources can be done using measurements of radiocarbon in CO<sub>2</sub> ( $\Delta^{14}\text{CO}_2$ ), since CO<sub>2</sub>  
62 emitted from fossil fuel combustion is devoid of <sup>14</sup>CO<sub>2</sub> due to radioactive decay (Levin et al.,  
63 2003).

64 Recent studies have shown that both simulated (Fischer et al. 2017) and observed (Graven et al.  
65 2018) measurements of  $\Delta^{14}\text{CO}_2$  at a network of sites could be used to estimate monthly mean  
66 California ffCO<sub>2</sub> emissions in a regional inversion with posterior uncertainties of ~5-8%, levels  
67 that are useful for the evaluation of bottom-up ffCO<sub>2</sub> emissions estimates. Furthermore, Graven  
68 et al., 2018 found their posterior emissions estimates were not significantly different from the  
69 California Air Resources Board’s reported ffCO<sub>2</sub> emissions, providing tentative validation of  
70 California’s reported ffCO<sub>2</sub> emissions in 2014-15. In another study using aircraft-based  $\Delta^{14}\text{CO}_2$   
71 measurements, Turnbull et al. (2011) found ffCO<sub>2</sub> emissions from Sacramento County in  
72 February 2009 were broadly consistent (mean difference of -17%, range: -43% to +133%) with  
73 the Vulcan emissions estimate (Gurney et al., 2009).



74 Although atmospheric inversions may provide a method for estimating emissions that is useful  
75 for evaluating emissions reduction policies, such as AB-32, systematic errors can arise from the  
76 atmospheric transport and prior emission models (e.g., Nassar et al., 2014; Liu et al., 2014;  
77 Hungershoefer et al., 2010; Chevallier et al., 2009, Gerbig et al., 2003). Comparisons of CO<sub>2</sub>  
78 simulated by different transport models have been conducted globally (e.g. Gurney et al., 2003,  
79 Peylin et al. 2013), and on the European continental scale (Peylin et al., 2011). The latter found  
80 that transport model error resulted in differences in modelled ffCO<sub>2</sub> concentrations that were 2-3  
81 times larger than using the same transport model but different prior emissions, depending on the  
82 location and time of year. However, comparisons of ffCO<sub>2</sub> simulated by different high resolution  
83 models (25 km or less) at regional scales are still lacking.

84 The objective of this paper is to examine the sensitivity of a regional inversion for Californian  
85 ffCO<sub>2</sub> emissions to errors in the prior emissions estimate and transport model. We build on  
86 previous work by Fischer et al. (2017) that developed an Observation System Simulation  
87 Experiment to estimate the uncertainties in both California statewide ffCO<sub>2</sub> emissions and  
88 biospheric fluxes that might be obtained using an atmospheric inversion. Their inversion was  
89 driven by a combination of in situ tower measurements, satellite column measurements from  
90 OCO-2, prior flux estimates, a regional atmospheric transport modelling system, and estimated  
91 uncertainties in prior CO<sub>2</sub> flux models, ffCO<sub>2</sub> measurements using radiocarbon, OCO-2  
92 measurements, and in atmospheric transport. In contrast to Fischer et al., 2017 we focus only on  
93 ffCO<sub>2</sub> emissions and use a network of flask samples without incorporating satellite  
94 measurements.

95 Our approach is to use simulation experiments to quantify representation and transport error  
96 using the inversion setup and the observation network from Graven et al. (2018) as a test case.



97 Specifically we test whether the inversion can estimate the “true” emissions that were used to  
98 produce the pseudo data, within the uncertainties, when the prior emissions estimate includes  
99 spatial and temporal representation errors within the scope of current emissions estimates  
100 (Vulcan v2.2 and EDGAR v4.2 FT2010). We further test whether the inversion can estimate  
101 “true” emissions, within the uncertainties, when the transport model used for the prior simulation  
102 is different from the transport model used to produce the pseudo data, emulating transport error.

## 103 **2. Data and Methods**

104 The analysis approach applies a Bayesian inversion developed from previous work that combines  
105 atmospheric observations, atmospheric transport modelling, prior flux models, and an  
106 uncertainty specification (Jeong et al., 2013; Fischer et al., 2017). Here, the inversion scales prior  
107 emission estimates in 15 regions (Figure 1a, Table 1) termed “air basins”, classified by the  
108 California Air Resources Board for air quality control  
109 (<https://www.arb.ca.gov/desig/adm/basincnty.htm>).

### 110 **2.1 Observation Network**

111 As a test case to explore uncertainties in ffCO<sub>2</sub> inversions, we use the observation network of 9  
112 tower sites in California that was used to collect flask samples for measurements of CO<sub>2</sub> and  
113 radiocarbon in CO<sub>2</sub> in 2014-15 (Figure 1a) (Graven et al. 2018). Three month-long campaigns  
114 were conducted in May 2014, October-November 2014 and January-February 2015, with flasks  
115 sampled approximately every 2-3 days at 22:30 GMT (14:30 local standard time). The time of  
116 observation was chosen as the planetary boundary layer is usually deepest in the afternoon so  
117 that errors in the modelled boundary layer concentration are considered smaller (Jeong et al.,  
118 2013), and afternoon concentrations are more representative of large regions.



119 The observed ffCO<sub>2</sub> concentration at a given site can be calculated by (Levin et al., 2003;  
120 Turnbull et al. 2009):

$$121 \quad ffCO_2 = C_{obs} \left( \frac{\Delta_{bg} - \Delta_{obs}}{\Delta_{bg} - \Delta_{ff}} \right) + \beta \quad (1)$$

122 Where C<sub>obs</sub> is the total observed CO<sub>2</sub> concentration at a given site. Δ refers to Δ<sup>14</sup>C, the ratio of  
123 <sup>14</sup>C/C reported in part per thousand deviation from a standard ratio, including corrections for  
124 mass-dependent isotopic fractionation and sample age (Stuiver and Polach, 1977). Δ<sub>bg</sub>, Δ<sub>obs</sub> and  
125 Δ<sub>ff</sub> are the Δ<sup>14</sup>CO<sub>2</sub> of background, observed and fossil fuel CO<sub>2</sub>, respectively, where Δ<sub>ff</sub> is -  
126 1000‰ since ffCO<sub>2</sub> is devoid of <sup>14</sup>CO<sub>2</sub>. The term β is a correction for the effect of other  
127 influences on Δ<sup>14</sup>CO<sub>2</sub>, principally heterotrophic respiration (Turnbull et al. 2009). Following  
128 Fischer et al. (2017), total observational uncertainty for ffCO<sub>2</sub> was assumed to be 1.5 ppm (1-σ).  
129 This is consistent with Graven et al. (2018), who estimated total uncertainty in ffCO<sub>2</sub> for  
130 individual samples of 1.0 to 1.9 ppm.

## 131 **2.2 Prior Emissions Estimates and Prior Uncertainty**

132 The two prior emissions estimates used here are gridded products produced by EDGAR (version  
133 FT2010) (EDGAR, 2011) for the year 2008 and Vulcan (version 2.2) for 2002 (Gurney et al.,  
134 2009). EDGAR is produced at an annual resolution whilst Vulcan has an hourly resolution. The  
135 two models use different emissions data and different methods to spatially allocate emissions  
136 with annually averaged statewide emissions differing by 17.8 TgC (~19% of mean emissions),  
137 and up to 11.6 TgC for individual air basins of California (Table 1). Although our campaigns  
138 took place in 2014-2015, we use emissions estimates from Vulcan for the year 2002 and EDGAR  
139 for 2008 as emissions estimates are not available from Vulcan and EDGAR for 2014-15. The



140 difference in state total emissions between 2002, 2008 and 2014-15 is 3-6 TgC (CARB, 2017),  
141 much less than the EDGAR-Vulcan difference of 17.8 TgC.

142 We estimate prior uncertainty in the same way as in Fischer et al. (2017), using a comparison of  
143 four gridded emissions estimates in California (Vulcan v2.2, EDGAR FT2010, ODIAC v2013  
144 and FFDAS v2) as well as a comparison across an ensemble of emissions estimates for one  
145 model (FFDAS v2, Asefi-Najafabady et al., 2014). The relative 1- $\sigma$  standard deviation is between  
146 8% and 100% for individual air basins (Table 1), and this is what we use to specify the 1- $\sigma$   
147 uncertainty in the prior emissions from each air basin. This estimate of prior uncertainty is  
148 referred to as “SD prior uncertainty”. We also conduct tests with an alternative prior uncertainty  
149 of 70% for each air basin (referred to as “70% prior uncertainty”). This was done to test the  
150 sensitivity of our results to the choice of prior uncertainty. Emissions occurring outside  
151 California were assumed to have an uncertainty of 100% for both cases.

### 152 **2.3 Atmospheric Transport Models**

153 We simulate ffCO<sub>2</sub> using three different atmospheric transport models outlined in Table 2. These  
154 models are commonly used in regional atmospheric transport modelling and greenhouse gas  
155 inversion studies but to date have not been compared in California. Two of the transport models  
156 use different versions and parameterizations of the Weather Research and Forecast (WRF) model  
157 combined with the Stochastic Time-Inverted Lagrangian Transport (STILT) model. The third  
158 transport model uses meteorology from the UK Met Office’s Unified Model (UM) combined  
159 with the Numerical Atmospheric dispersion Modelling Environment (NAME).

160 The first WRF-STILT model is run at Lawrence Berkeley National Laboratory (WS-LBL,  
161 Fischer et al. 2017; Jeong et al. 2016; Bagley et al. 2017) and uses WRF version 3.5.1 (Lin,



162 2003; Nehr Korn et al., 2010). Estimates for Planetary Boundary Layer Height (PBLH) are based  
163 on the Mellor–Yamada–Nakanishi–Niino version 2 (MYNN2) parameterization (Nakanishi and  
164 Niino 2004, 2006). As in Jeong et al. (2016), Fischer et al. (2017) and Bagley et al. (2017), two  
165 land surface models (LSMs) are used depending on the location of the observation site. A 5-layer  
166 thermal diffusion land surface model is used in the Central Valley for the May campaign whilst  
167 the Noah LSM (Chen et al., 2001) is used in the remaining campaigns and regions of California.  
168 We implement multiple nested domains, with the outermost domain spanning 16–59°N and 154–  
169 137°W with a 36km resolution, a second domain of 12km resolution over western North  
170 America, and a third domain of 4km resolution over California. Two urban domains of 1.3 km  
171 resolution are used in the San Francisco Bay area and the metropolitan area of Los Angeles.  
172 Footprints describing the sensitivity of an observation to surface emissions are calculated by  
173 simulating 500 model particles and tracking them backward for 7 days. The footprint of a given  
174 site and observation time is produced hourly for particles below 0.5 times the PBLH.

175 The second WRF-STILT model is from CarbonTracker-Lagrange (WS-CTL), an effort led at  
176 NOAA to produce standard footprints for greenhouse gas observation sites in North America  
177 (<https://www.esrl.noaa.gov/gmd/ccgg/carbontracker-lagrange>). WS-CTL uses WRF version  
178 2.1.2 and the Yonsei University (YSU) (Hong et al., 2006) PBLH scheme coupled with the Noah  
179 land surface model and the MM5 (fifth generation Pennsylvania State University-National  
180 Center for Atmospheric Research Mesoscale Model, Grell et al., 1994) similarity theory-based  
181 surface layer scheme. As with WS-LBL, simulations are run for 7 days and particles below 0.5  
182 times the PBLH are used in the calculation of the footprint. Footprints have a spatial resolution  
183 of 0.1° for the first 24 hours and 1° for the remaining 6 days. Footprints are hourly dis-  
184 aggregated for the first 24 hours and then aggregated for the remaining 6 days. The 0.1° spatial





185 resolution domain is  $31^\circ$  longitude by  $21^\circ$  latitude with the domain centered on the release  
186 location. The  $1^\circ$  resolution has a domain of  $170^\circ\text{E}$  to  $50^\circ\text{E}$  longitude and  $10^\circ\text{N}$  to  $80^\circ\text{N}$  latitude.  
187 The WRF domain covers most of continental North America (Fig. 1 in Nehr Korn et al., 2010)  
188 with 30 km resolution and has a finer nest with 10 km spatial resolution over the continental  
189 United States. WS-CTL simulates footprints for 500 particles released over a 2-hour period  
190 between 21:00 and 23:00 GMT (13:00 and 15:00 PST). An exception is Sutro Tower (STR),  
191 where footprints are only available for an instantaneous release of 500 particles at 22:10 GMT.  
192 Walnut Grove (WGC) footprints are available only for a release height of 30m a.g.l, which is  
193 lower than the sampling height of 91m a.g.l. used in the observation campaign (Graven et al.  
194 2018) and used in the other two transport models. Footprints were available for 2014 but not for  
195 2015, so the WS-CTL model is used for simulations of the May and Oct-Nov 2014 campaigns  
196 but not for the Jan-Feb 2015 campaign.

197 The third model, UM-NAME, is the UK Met Office's NAME model, Version 3.6.5 (Jones et al.,  
198 2007), driven by meteorology from the Met Office's global numerical weather prediction model,  
199 the Unified Model (UM) (Cullen et al., 1993). The UM model has a horizontal resolution of  $\sim 25$   
200 km up to July 2014, covering the period of the May 2014 campaign. The horizontal resolution  
201 was then increased to  $\sim 17$  km covering both the October-November 2014 and January-February  
202 2015 campaigns. The temporal resolution of the UM meteorology is every 3 hours for all  
203 campaigns. Following a similar approach as for the WRF-STILT models, 500 particles were  
204 released instantaneously at 22:30 GMT and simulated for hourly dis-aggregated footprints for the  
205 first 24 hours and aggregated for the remaining 6 days. The footprints are calculated for the same  
206 horizontal resolution as the UM meteorology (25 or 17km), where the particles present in the



207 layer between 0 and 100 m above ground level are used to calculate the footprint. The  
208 computational domain covers 175.0°W to 75°W longitude and 6.0°N to 74°N latitude.

209 Simulated ffCO<sub>2</sub> signals (the enhancement of CO<sub>2</sub> concentration due to ffCO<sub>2</sub> emissions within  
210 the model domain) are calculated by taking the product of the footprint and an emissions  
211 estimate. Following previous work, we assume a transport model uncertainty of 0.5 times the  
212 mean monthly signal in the pseudo-observations at each site (Jeong et al., 2013; Fischer et al  
213 2017).

214 Ten ensembles were run for UM-NAME to test the effect of random errors on the calculation of  
215 the footprint. The RMSE was within 10% of the mean monthly signal for most observation sites.  
216 This is similar to the findings of Jeong et al. (2012), which the transport model uncertainty is  
217 based on. Two observation sites (THD and VTR) had slightly higher RMSE, but both were  
218 within 20% of the mean monthly signal.

## 219 **2.4 Inversion Method**

220 Our inversion method is a Bayesian synthesis inversion to scale emissions in separate regions of  
221 California. We follow the same approach as Fischer et al. (2017) to solve for a vector of scaling  
222 factors,  $\lambda$ , for 15 air basins and a 16<sup>th</sup> region representing the area outside of California. Unlike  
223 Fischer et al. (2017), we do not split the San Joaquin Valley into two regions. The inversion uses  
224 the set of observations,  $c$ , and the matrix of predicted ffCO<sub>2</sub> signals from each air basin,  $K$ , to  
225 optimize the cost function  $J$ :

$$226 \quad J_{\lambda} = (c - K\lambda)^T R^{-1} (c - K\lambda) + (\lambda - \lambda_{prior})^T Q_{\lambda}^{-1} (\lambda - \lambda_{prior}) \quad (2)$$

227  $\lambda_{prior}$  is the prior estimate of the scaling factors (a vector of ones with length equal to the number  
228 of regions) and  $R$  and  $Q_{\lambda}$  are the error covariance matrices relating to observational and model



229 transport errors, and prior emissions estimate errors respectively. The non-diagonal elements of  
230  $\mathbf{R}$  and  $\mathbf{Q}_\lambda$  are zero, assuming uncorrelated errors in the prior emissions in each air basin and in  
231 the model and observations. This assumption for  $\mathbf{R}$  is robust as we only generate one pseudo  
232 observation every 2-3 days. Included in  $\mathbf{R}$  are observational errors and transport model errors,  
233 added in quadrature. Therefore if the average signal at an observation site is very small, then  
234 observational uncertainty (1.5 ppm) will dominate  $\mathbf{R}$ . Minimizing  $J$  using the standard least  
235 squares formulation under the assumption of Gaussian distributed uncertainties gives the  
236 posterior estimate for  $\lambda$  following:

$$237 \quad \lambda_{post} = (\mathbf{K}^T \mathbf{R}^{-1} \mathbf{K} + \mathbf{Q}_\lambda^{-1})^{-1} (\mathbf{K}^T \mathbf{R}^{-1} \mathbf{c} + \mathbf{Q}_\lambda^{-1} \lambda_{prior}) \quad (3)$$

238 With the posterior error covariance given as:

$$239 \quad V_{post} = (\mathbf{K}^T \mathbf{R}^{-1} \mathbf{K} + \mathbf{Q}_\lambda^{-1})^{-1} \quad (4)$$

240  $\lambda_{post}$  and  $V_{post}$  are computed separately for each of the three campaigns outlined in section 2.1.

241 Posterior emissions estimates are the product of  $\lambda_{post}$  and the prior emissions estimate from each  
242 air basin. State total emissions are then calculated by summing the emissions in each air basin.

243 Uncertainty in the state-wide Californian posterior flux, including error correlations, is calculated  
244 as:

$$245 \quad \sigma_E^2 = \mathbf{E}_{prior} V_{post} \mathbf{E}_{prior}^T \quad (5)$$

246 Where  $\mathbf{E}_{prior}$  is a vector of ffCO<sub>2</sub> emissions from each air basin.

## 247 **2.5 Simulation Experiments**

248 We conduct a series of experiments to test the performance of the inversion in estimating the true  
249 emissions when the emissions estimates or transport models used to produce pseudo-  
250 observations are different to those used to produce the prior simulations. The tests explore the



251 effect differences in the magnitude, spatial distribution, and temporal variation of prior emissions  
252 have on posterior emissions. We also examine the effect of using different transport models to  
253 simulate pseudo observations and to simulate prior concentrations.

254 As part of these experiments, we evaluate the impact of outlier removal on the simulation  
255 experiments. Outlier removal is generally used in atmospheric inversions when there is an issue  
256 with the ability of the model to simulate a particular observation. We use the outlier removal  
257 method outlined in Graven et al. (2018) and compare with inversion results where no outliers are  
258 removed. In this outlier removal method, an observation (here, a pseudo-observation) is  
259 designated as an outlier if (1) the absolute difference between the  $\text{ffCO}_2$  signals in the  
260 observation and the prior simulation is greater than the average of the observed and simulated  
261  $\text{ffCO}_2$ , and (2) either the observed or simulated  $\text{ffCO}_2$  is greater than 5 ppm.

### 262 **2.5.1 Difference in magnitude of emissions**

263 First we test how well the inversion estimates the true emissions if the prior emissions have a  
264 systematic error in magnitude, but no error in the spatial or temporal distribution of emissions  
265 and no error in atmospheric transport. In this experiment, the prior emissions estimate is given by  
266 EDGAR and the true  $\text{ffCO}_2$  signals were generated by scaling the EDGAR emissions in each air  
267 basin to match the annually averaged Vulcan emissions in that air basin. These differences range  
268 from 0.1 TgC in San Diego to 11.6 TgC in the San Joaquin Valley (Table 1). The EDGAR state  
269 total emissions are 12% higher than Vulcan, so the bias in the prior estimate in the state total  
270  $\text{ffCO}_2$  emissions is +12%. The experiment is run for all the transport models with no temporal  
271 variation in emissions. This experiment assesses the performance of the inversion and the



272 strength of the data constraint provided by the observation network in the simplest case where  
273 there are regional errors in the magnitude of prior emissions.

### 274 **2.5.2 Difference in spatial distribution of emissions**

275 To investigate the bias in the posterior emissions estimate that could result from errors in the  
276 spatial distribution of prior emissions within each air basin, we now use annually averaged  
277 Vulcan emissions as the true emissions and EDGAR emissions scaled in each air basin to match  
278 the annually averaged Vulcan emissions in that region as the prior estimate of emissions. In this  
279 experiment, the prior estimate of the total emissions in each air basin is unbiased, and we assess  
280 how differences in the spatial distribution of emissions between Vulcan and EDGAR in each air  
281 basin may lead to a bias in the posterior emissions estimate. As shown in Figure 1c, the most  
282 significant discrepancies in spatial distribution are in the major urban areas of Los Angeles and  
283 the San Francisco Bay. This experiment is also run for all the transport models using the same  
284 transport model for both the true and prior simulation and including no temporal variation in  
285 emissions.

### 286 **2.5.3 Difference in temporal variation of emissions**

287 To assess the impact of temporally-varying emissions on the inversion result, we generated true  
288  $\text{ffCO}_2$  signals with temporally-invariant annually-averaged Vulcan emissions and prior  $\text{ffCO}_2$   
289 signals with temporally-varying Vulcan emissions. We scaled the temporally-varying Vulcan  
290 emissions in each air basin so that the total  $\text{ffCO}_2$  emissions were the same magnitude as the total  
291  $\text{ffCO}_2$  emissions in the annually averaged Vulcan emissions for each field campaign. As shown  
292 in Figure 1d, scaling was less than 10% of annual mean emissions with campaigns occurring  
293 during maxima and minima of the annual emissions cycle. Here the prior estimate is again



294 unbiased, and we assess how differences in the diurnal variation of emissions (see Fig 1b) may  
295 lead to a bias in the posterior emissions estimate. This experiment is also run for all the transport  
296 models using the same transport model for both the true and prior simulation.

### 297 **2.5.4 Difference in Atmospheric Transport**

298 To test the effect of differences in the simulated atmospheric transport of emissions, the same  
299 emissions estimate (annually-averaged Vulcan) is coupled with two different transport models to  
300 generate prior and true ffCO<sub>2</sub> signals. This experiment investigates potential effects of transport  
301 errors, within the variations in transport across the three models we use. WS-LBL is considered  
302 the “true” atmospheric transport while UM-NAME and WS-CTL are used for the prior  
303 simulation in individual experiments. Here the prior estimate is again unbiased, and we assess  
304 how differences in the modeled atmospheric transport may lead to a bias in the posterior  
305 emissions estimate.

## 306 **3 Results**

### 307 **3.1 Simulated ffCO<sub>2</sub> Observations**

308 Before presenting the results of the inversion experiments, we first examine simulated ffCO<sub>2</sub>  
309 contributions from different regions at each of the 9 observation sites. This allows us to quantify  
310 which air basins have the largest influence on simulated concentrations at observation sites and  
311 better interpret the results of the experiments. Figure 2 shows simulated concentrations at  
312 observation sites resulting from emissions in the 6 highest-emitting air basins in California, and  
313 from outside California. The highest signals (> 10 ppm) are simulated at urban sites (e.g. CIT  
314 and SBC) for emissions from urban air basins (e.g., South Coast, 14.SC). The 9 air basins not  
315 shown in Fig. 2 contributed signals below 0.1 ppm due to the small size or low emissions of the



316 air basin (e.g. Lake County and Lake Tahoe), or distance from the observation network (e.g.  
317 Northeast Plateau, Great Basin Valleys and Salton Sea). In general, the northern sites (THD to  
318 SLT in Fig 2) are sensitive to northern air basins (Sacramento and San Joaquin Valleys and SF  
319 Bay), and the southern sites (VTR to SIO) are sensitive to emissions from southern air basins  
320 (Mojave Desert, South Coast and San Diego). All transport models show the observation sites  
321 are sensitive to more air basins in the Oct-Nov and Jan-Feb campaigns, compared to the May  
322 campaign (Fig. 2). Signals simulated by WS-CTL come from fewer air basins than UM-NAME  
323 or WS-LBL, particularly in May.

324 In our simulation experiments, signals from outside California are generally small compared to  
325 the total signal for most sites (<10% on average), although they can average 20-50% for STB,  
326 STR, SLT and SIO for individual campaigns. For THD, located near the northern border of the  
327 state, a larger influence from outside California is found, 10-90%, due to a combination of  
328 relatively low local emissions and northerly winds transporting emissions from the northwestern  
329 United States and Canada .

### 330 **3.2.1 Difference in magnitude of emissions**

331 Figure 3 (a) shows the statewide inversion result for the experiment testing the effect of a bias in  
332 magnitude in regional emissions in the prior simulation. In this figure, and similar figures that  
333 follow for the other experiments, prior estimates are represented by black markers and posterior  
334 estimates are represented by colored markers, with the  $2\text{-}\sigma$  uncertainty on the x-axis and the bias  
335 relative to the truth on the y-axis. The diagonal lines show 1:1 and 1:-1 lines, so that a marker  
336 lying to the right of these lines indicate the posterior bias is smaller than the posterior  
337 uncertainty, whereas a marker to the left of these lines indicate the posterior bias is larger than



338 the posterior uncertainty. Filled markers show results using SD prior uncertainty and empty  
339 markers show results using 70% prior uncertainty. Prior and posterior uncertainties are expressed  
340 as  $2\text{-}\sigma$ .

341 For all transport models and campaigns, the inversion is able to reduce prior bias and scale  
342 posterior emissions towards the truth. The +12% bias in the statewide emissions in the prior was  
343 reduced to a posterior bias of between 0 and +9% (mean bias = +5%) for SD prior uncertainty.  
344 Using 70% prior uncertainty reduced prior bias to between -3 and +6 (mean = +1%). Statewide  
345 posterior uncertainty was 10-14% (mean 12%) and 14-32% (mean = 21%) for SD and 70% prior  
346 uncertainty respectively, where uncertainty is expressed as  $2\text{-}\sigma$ , lower than the statewide prior  
347 uncertainties of 16% for SD and 69% for 70% prior uncertainty. There were no outliers  
348 identified in this experiment.

349 To determine what is driving the statewide results, we examine the individual air basin inversion  
350 results. Figure 3 (b) shows the inversion results for the six main emission regions of California,  
351 with San Joaquin Valley (8.SJV) and South Coast (14.SC) having the largest prior biases. For the  
352 San Joaquin Valley (8.SJV) and South Coast (14.SC) regions with the largest prior bias, the  
353 biases are reduced in most cases, however, only the posterior estimates from the 70% prior  
354 uncertainty experiment overlap the true emissions. The posterior estimates for SD prior  
355 uncertainty do not overlap with the truth, indicating that the  $2\text{-}\sigma$  prior uncertainty of 24% in  
356 South Coast (14.SC), for example, restricts the inversion from eliminating biases of 30% in these  
357 regions (Table 1), given the observations available. The 9 air basins omitted from Fig. 3(b) are  
358 generally not being scaled by the inversion due to a lack of constraint from the observation  
359 network, low emissions, or small prior uncertainty (Figure S1).





360 The bias in the posterior estimate of statewide emissions is larger in May than in Oct-Nov and  
361 Jan-Feb (Fig 3a, triangles). This poorer performance of the inversion in May can be largely  
362 attributed to the San Joaquin Valley (8.SJV), where the posterior emissions are largely  
363 unchanged from the prior in May. There is no observation site in the San Joaquin Valley, and as  
364 shown in Fig. 2, emissions in the San Joaquin Valley do not reach observation sites in  
365 neighboring air basins in May, but they do reach these sites in Oct-Nov and Jan-Feb. In contrast,  
366 the South Coast (14.SC) influences the two observation sites, CIT and SBC, located in the region  
367 as well as several other sites (Fig. 2). Both CIT and SBC show prior signals are too high  
368 compared to true signals for all campaigns and models (Fig. 3c), reflecting the positive bias in  
369 prior emissions in the South Coast region, which is reduced in the posterior.

### 370 **3.2.2 Difference in spatial distribution of emissions**

371 The statewide inversion results for the experiment including errors in the spatial distribution of  
372 emissions are shown in Figure 4 (a). In this case the magnitude of prior emissions in each air  
373 basin is equal to true emissions and we aim to quantify how errors in the spatial distribution of  
374 emissions (EDGAR as prior and Vulcan as true distribution) lead to bias in posterior emissions  
375 estimates. Posterior emissions are negatively biased, apart from WS-LBL in January-February.  
376 Posterior bias was between -10% and +1% (mean -4%) for SD prior uncertainty and between -  
377 10% and +4% (mean = -4%) for 70% prior uncertainty across transport models and campaigns.  
378 As might be expected from the experimental setup with an unbiased prior, posterior emissions  
379 estimates generated using SD prior uncertainty have a smaller mean bias and smaller range of  
380 posterior estimates compared to those generated using 70% prior uncertainty. Statewide  
381 uncertainty was reduced from 16% to 10-14% (mean = 12%) for SD prior uncertainty and from  
382 58% to 14-21% (mean = 18%) for 70% air basin prior uncertainty. Biases induced are smaller



383 than the 2- $\sigma$  posterior uncertainty across all transport models, campaigns and choice of prior  
384 uncertainty.

385 Posterior emissions results in the two largest emitting air basins (the San Francisco Bay and  
386 South Coast) are also negatively biased in most cases (Fig 4b). In several cases, posterior biases  
387 are larger than the associated posterior uncertainties, for example in the South Coast for WS-  
388 LBL in all cases. Considering Figure 4 (c), prior ffCO<sub>2</sub> signals are being overestimated more  
389 often than underestimated, particularly for the relatively more urban sites CIT and SLT.  
390 Sacramento Valley (3.SV) and the San Joaquin Valley (8.SJV) have higher posterior emissions  
391 in WS-LBL in most cases, possibly due to the inversion compensating for reduced posterior  
392 emissions in the San Francisco Bay (13.SFB) and South Coast (14.SC).

393 Since the prior emissions from EDGAR have been scaled to have the same total as Vulcan (the  
394 true emissions) in each region, the pattern of more negative posterior emissions is only caused by  
395 the sub-regional spatial distribution of emissions. Comparing Vulcan and EDGAR native grid  
396 cell emissions in Figures 1c and S2, EDGAR tends to have greater emissions in high-emission  
397 grid cells. In other words, the emissions are more concentrated in EDGAR and more dispersed in  
398 Vulcan. This pattern explains the negative bias in posterior emissions for the urban South Coast  
399 air basin. The opposite effect does not appear to hold for rural observation sites and regions,  
400 perhaps because rural emissions are already rather dispersed and have less of an influence on the  
401 observations.

402 In these experiments, 0-3% of observations were identified as outliers, but excluding outliers did  
403 not change the statewide result significantly (<1% change in mean bias).

### 404 **3.2.3 Difference in temporal variation of emissions**



405 Figure 5 (a) shows the statewide inversion result for the experiment where the emissions are  
406 Vulcan temporally-varying in the prior simulation (see Fig. 1b) but Vulcan temporally-invariant  
407 in the true simulation. Posterior bias was between -13 and +5% (mean = -3%) for SD uncertainty  
408 and between -15% and +6% (mean = -3%) for 70% prior uncertainty. Posterior uncertainty was  
409 11-15% (mean = 12%) for SD prior uncertainty and 15-24% (mean = 18%) in posterior  
410 emissions for SD (70%) prior uncertainty. Outlier removal resulted in 0-1% (mean = 0%) of data  
411 points being removed, which did not change the statewide results.

412 The posterior estimate for WS-LBL in May with SD prior uncertainty has a significant negative  
413 bias of -13%, approximately the same magnitude as the associated 2- $\sigma$  posterior uncertainty. As  
414 can be seen by the air basin results of Figure 5 (b), the statewide bias for WS-LBL in May is  
415 being driven by a large regional bias in the South Coast, but also in the San Francisco Bay and  
416 San Diego air basins. These regional biases are larger than their associated posterior  
417 uncertainties. Figure 5 (c) shows the prior ffCO<sub>2</sub> signals at CIT average ~7ppm too high in May  
418 for WS-LBL. In contrast, prior ffCO<sub>2</sub> signals at CIT and SBC are too low in Oct-Nov for WS-  
419 CTL, leading to a high bias in posterior emissions from the South Coast. San Diego also  
420 exhibited both high and low biases in the posterior emissions. Overall, temporal variations in  
421 emissions led to posterior biases generally within  $\pm 6\%$ , but as large as 15%; however, a  
422 consistent pattern in the posterior bias due to the temporal representation in emissions was not  
423 found.

#### 424 **3.2.4 Difference in Atmospheric Transport**

425 The statewide inversion results for the experiment where the atmospheric transport in the prior  
426 simulation uses WS-CTL or UM-NAME but the atmospheric transport in the true simulation



427 uses WS-LBL are shown in Figure 6 (a). Outliers were identified in these experiments and we  
428 present results for inversions including all data and for inversions where outliers were removed.

429 When all data are included, differences in atmospheric transport model introduces a bias in  
430 statewide posterior emissions of between -42% and -3% (mean = -12%) for SD prior uncertainty  
431 and between -32% and 0% (mean = -15%) for 70% prior uncertainty. For one case, using WS-  
432 CTL to generate prior signals in October-November, the bias in the posterior emissions estimate  
433 was larger than the  $2\text{-}\sigma$  uncertainty for both SD and 70% prior uncertainty.

434 Removing outliers significantly improved the inversion results (Figure 6 b): the mean bias was  
435 between -10% and 0% (mean = -3%) for SD prior uncertainty and between -9% and +6% (mean  
436 = -5%) for 70% prior uncertainty when outliers were removed. Posterior uncertainty was 9-15%  
437 (mean = 12%) and 15-24% (mean = 18%) for SD and 70% prior uncertainty respectively, with  
438 all posterior estimates within  $2\text{-}\sigma$  of the true statewide emissions. The reduction in posterior bias  
439 when outliers are removed is mostly due to the removal of a few large positive outliers in prior  
440 simulated signals by WS-CTL (Figure 7). Figure 7 illustrates the time series of simulated  $\text{ffCO}_2$   
441 in each model with outliers shown as an x. Outliers removed were between 6.9% and 20.6% of  
442 all observations (mean = 10.5%). This is similar to the fraction of outliers identified in Graven et  
443 al. 2018 using the same method with real data (~8%). It is also similar to that of Jeong et al.,  
444 2012a and b (0-27%) for monthly inversions of  $\text{CH}_4$  in California using a different method of  
445 identifying outliers where model-data residuals are larger than  $3\text{-}\sigma$  of model-data uncertainty.

446 While the statewide posterior emissions estimate is significantly biased in only one case (WS-  
447 CTL in Oct-Nov) when outliers are not removed, the posterior emissions estimates for the main  
448 emissions regions are significantly biased in several cases (Fig 6c). The largest bias is in the



449 South Coast region where posterior estimates are biased by more than -75% (with 1% posterior  
450 uncertainty) in Oct-Nov when using WS-CTL to generate prior signals. This large posterior  
451 emissions bias in the South Coast and the statewide total can be attributed to overestimates in  
452 prior ffCO<sub>2</sub> signal of more than 6ppm on average at CIT and SBC and more than 2ppm at WGC  
453 and STR (Fig. 6e) due to some high outliers in the WS-CTL simulations (Fig. 7). Posterior  
454 estimates for San Francisco Bay, South Coast and San Diego were also significantly biased in  
455 some other cases, particularly for 70% prior uncertainty but also for SD prior uncertainty. This  
456 indicates that regional biases caused by differences in atmospheric transport appear to  
457 compensate over the statewide scale, and that results for individual regions are less robust than  
458 aggregate results for the statewide network. It also suggests that a dense observation network is  
459 beneficial to reducing the impact of uncertainty in atmospheric transport.

460 To investigate the differences in simulated ffCO<sub>2</sub> and assess whether these could be attributed to  
461 specific aspects of modelled meteorology, we compared PBLH and wind speed in WS-LBL and  
462 the UM for 5 of the 9 observation sites where PBLH output was available. PBLH was not  
463 available for WS-CTL. Estimates for PBLH in WS-LBL are based on the Mellor–Yamada–  
464 Nakanishi–Niino version 2 (MYNN2) parameterization scheme that estimates PBLH using  
465 localized turbulence kinetic energy closure parameterization (Nakanishi and Niino 2004, 2006).  
466 Estimates of PBLH are calculated internally within the UM. PBLH and wind speed were  
467 averaged over 6 hours from 12 to 6pm Pacific Standard Time to compare the afternoon means  
468 (Seibert et al., 2000). We found no consistent correlation between differences in PBLH or wind  
469 speed and differences in simulated ffCO<sub>2</sub> between models across sites and campaigns (Figure  
470 S3). Absolute values of wind direction and ffCO<sub>2</sub> did not show consistent correlations either. The



471 lack of correlation suggests we cannot attribute differences in simulated ffCO<sub>2</sub> to any single  
472 meteorological variable estimated at any individual station in the transport models.

473 We also examined if differences in simulated ffCO<sub>2</sub> signals across transport models could be  
474 explained by the differences in spatial resolution of the models. WS-CTL footprints were re-  
475 gridded from a 0.1° native grid to the coarser UM-NAME grid of 17 or 25km and then used to  
476 simulate ffCO<sub>2</sub>. For this comparison, we simulated ffCO<sub>2</sub> every day over the campaign period.  
477 We found no consistent reduction in mean ffCO<sub>2</sub> bias between sites over the 2 campaigns,  
478 however there is a reduction in spread of bias at 4 sites for both campaigns (WGC, SLT, SBC  
479 and SIO), suggesting model resolution could potentially have an impact for these sites. In general  
480 however, we cannot say that transport model resolution error in atmospheric transport is a key  
481 driver of ffCO<sub>2</sub> signal bias across observation sites (Figure S4).

#### 482 **4 Discussion**

483 Our results show that atmospheric inversions can reduce a hypothetical bias in the magnitude of  
484 prior ffCO<sub>2</sub> emissions estimates for the U.S. state of California using the ground-based  
485 observation network from Graven et al. (2018), under the idealized assumptions of perfect  
486 atmospheric transport and perfect spatio-temporal distribution of emissions in the prior estimate.  
487 By exploring differences in model transport and spatio-temporal distribution of prior emissions,  
488 we found that biases of magnitude 1-15% in monthly posterior estimates of statewide emissions  
489 can result from differences in the temporal variation, spatial distribution and modelled transport  
490 of the prior simulation. However, these biases were less than the 2- $\sigma$  posterior uncertainty in  
491 state-total emissions, when outliers were removed. In some cases, the biases in posterior  
492 emissions for individual air basins were significant, compared to the posterior uncertainties,



493 suggesting that estimates for individual regions are less reliable than the aggregate estimates of  
494 the state-wide total.

495 The largest bias in statewide posterior estimates was found to be caused by errors in the temporal  
496 variation in emissions. This highlights the necessity for temporally-varying emissions to be  
497 estimated and included in prior emissions estimates, particularly for urban regions. Similar  
498 results have been found in other regions including Indianapolis (Turnbull et al. 2015) and Europe  
499 (Peylin et al. 2011), and more generally, for high-emission regions around the globe (Zhang et al.  
500 2016). Although the afternoon sampling is near to the diurnal maximum in emissions in  
501 California (Fig. 1c, Gurney et al. 2009), which might be expected to lead to higher simulated  
502 ffCO<sub>2</sub> in temporally-varying vs temporally-invariant emissions, we did not find consistently  
503 positive biases in ffCO<sub>2</sub> but rather both positive and negative biases. This suggests the overall  
504 impact of temporally-varying emissions depends on the model transport and the characteristics of  
505 the observation site. Furthermore, uncertainties in the temporal distribution of emissions at an  
506 hourly resolution have not yet been fully quantified (Nassar et al., 2013).

507 Errors in model transport, as represented in our experiments by using different transport models,  
508 were shown to bias posterior ffCO<sub>2</sub> emissions by 10% or less, when outliers were removed.  
509 These biases related to transport error are somewhat lower than estimated by similar simulation  
510 experiments for ffCO<sub>2</sub> emissions estimates for the U.S. by Basu et al. (2016) using different  
511 transport models (>10%), although their spatial scale was larger and the alternate model they  
512 used was intentionally biased. In contrast, the three models we use are all actively applied in  
513 regional greenhouse gas inversions. Our results are comparable to the estimate of ±15%  
514 uncertainty in atmospheric transport in WS-LBL using comparisons with atmospheric  
515 observations of CO in California (Bagley et al. 2017).



516 The fraction of pseudo-observations we identified as outliers in these transport error experiments  
517 (10.5%, range 6.9-20.6%), was similar to Graven et al., 2018, where 8% of all observations were  
518 removed as outliers using the same method. The outliers in our experiments were primarily high  
519 ffCO<sub>2</sub> signals simulated by WS-CTL in Oct-Nov. When included in the inversion, these did lead  
520 to significant biases in the posterior estimates for the experiment on model transport. This  
521 highlights the need for careful examination of simulated ffCO<sub>2</sub> and consideration of outliers in  
522 atmospheric ffCO<sub>2</sub> inversions.

523 Attributing differences in simulated ffCO<sub>2</sub> between the different transport models to specific  
524 meteorological variables proved inconclusive, and model resolution error did not appear to  
525 explain the differences in simulated signals, although we were not able to investigate aggregation  
526 error in comparison to the high-resolution WS-LBL model. Wang et al. (2017) found  
527 aggregation error to be only a minor contributor to errors in simulated ffCO<sub>2</sub> in Europe, while  
528 Feng et al., (2016) found that high-resolution gridded emissions estimates could be more  
529 important than high resolution transport models for simulations of greenhouse gases in Greater  
530 Los Angeles. We found that differences in the spatial representation of prior emissions in  
531 EDGAR compared to Vulcan led to consistently lower, although not significantly different,  
532 posterior state-wide estimates due to the emissions in EDGAR being more concentrated in urban  
533 regions. The spatial allocation of emissions between urban and rural regions in gridded emissions  
534 estimates have much larger uncertainties than national totals (Hogue et al. 2016), suggesting that  
535 several different gridded emissions estimates should be used in regional ffCO<sub>2</sub> inversions to  
536 capture this source of uncertainty.

537 The results of these experiments suggest that the choice of prior emissions estimate and transport  
538 model (among those considered here and currently used in the community) used in our ffCO<sub>2</sub>





539 inversion would result in differences of 15% or less in posterior state-wide ffCO<sub>2</sub> emissions in  
540 California, using the observation network from Graven et al. (2018). These differences are  
541 generally not significant, compared to the posterior 2- $\sigma$  uncertainties of 10 to 15%. In  
542 comparison, Graven et al. (2018) found that posterior state-wide ffCO<sub>2</sub> emissions were not  
543 statistically different when using temporally-varying emissions from Vulcan, as compared to  
544 annual mean emissions from Vulcan or EDGAR, with posterior uncertainties of  $\pm 15$  to  $\pm 17\%$ .  
545 Our results may be specific to the California region, observation network and inversion setup we  
546 consider here, but we expect that similar differences of 1-15% are likely to be found elsewhere in  
547 similar inversions at comparable regional scales.

548 In our results, emissions from many small or rural air basins did not have a significant  
549 contribution to the local enhancement of ffCO<sub>2</sub> at the observation sites and were not adjusted by  
550 the inversion in most cases (Figure 2, Figure S1). Combined with our experimental setup  
551 specifying the magnitude of prior emissions to be equal to true emissions, it might be expected  
552 that our results could underestimate the predicted biases in posterior emissions. However, these  
553 experiments were designed specifically to quantify representation and transport error using the  
554 inversion setup and the observation network from Graven et al. (2018) as a test case. Fischer et  
555 al. (2017), showed in individual simulation experiments that using either EDGAR or a spatially  
556 uniform flux of  $1 \mu \text{mol m}^{-2} \text{s}^{-1}$  as a biased prior produced posterior emissions that are  
557 substantially closer to true emissions, but only if the prior uncertainties are set large enough to  
558 encompass biases in prior emissions. Further experiments using a different experimental setup  
559 such as choice of mismatch error or specification of inversion regions (e.g. to change the  
560 inversion region size based on proximity to the observation network, Manning et al., 2011),



561 would help to characterize uncertainties in regional ffCO<sub>2</sub> inversions and the robustness of  
562 posterior estimates to the choices made in the inversion setup.

### 563 **Conclusion**

564 We have shown that atmospheric inversions for the U.S. state of California can reduce a  
565 hypothetical bias in the magnitude of prior emissions estimates of ffCO<sub>2</sub> in California using the  
566 ground-based observation network from Graven et al. (2018). Experiments to characterize the  
567 effect of differences in the spatial and temporal distribution in prior emissions resulted in biases  
568 in posterior state-total emissions with magnitudes of 1-15%, similar to monthly posterior  
569 estimates of Basu et al., 2016 for the western United States. Our results highlight the need for (1)  
570 temporal variation to be included in prior emissions, (2) different estimates of the spatial  
571 distribution of emissions between urban and rural regions to be considered, and (3)  
572 representation of atmospheric transport in regional ffCO<sub>2</sub> inversions to be further evaluated.

### 573 **Acknowledgments**

574 This project was funded by the Natural Environment Research Council (NERC, UK), the UK  
575 Met Office, NASA Carbon Monitoring System (NNX13AP33G and NNH13AW56I), and the  
576 European Commission through a Marie Curie Career Integration Grant. The authors thank A.  
577 Andrews and the CarbonTracker-Lagrange team for providing footprints. Support for  
578 CarbonTracker-Lagrange has been provided by the NOAA Climate Program Office's  
579 Atmospheric Chemistry, Carbon Cycle, & Climate (AC4) Program and the NASA Carbon  
580 Monitoring System.

### 581 **References**



- 582 R. J. Andres, T. A. Boden, F. M. Bréon, P. Ciais, S. Davis, D. Erickson, J. S. Gregg, A.  
583 Jacobson, G. Marland, J. Miller, T. Oda, J. G J Olivier, M. R. Raupach, P. Rayner, and K.  
584 Treanton. A synthesis of carbon dioxide emissions from fossil-fuel combustion.  
585 Biogeosciences, 9(5):1845–1871, 2012. ISSN 17264170. doi: 10.5194/bg-9-1845-2012.  
586
- 587 S. Asefi-Najafabady, P. J. Rayner, K. R. Gurney, A. McRobert, Y. Song, K. Coltin, J. Huang, C.  
588 Elvidge, and K. Baugh. A multiyear, global gridded fossil fuel CO<sub>2</sub> emission data product:  
589 Evaluation and analysis of results. Journal of Geophysical Research: Atmospheres,  
590 119(17):10,213–10,231, 2014.  
591
- 592 Sourish Basu, John Bharat Miller, and Scott Lehman. Separation of biospheric and fossil fuel  
593 fluxes of CO<sub>2</sub> by atmospheric inversion of CO<sub>2</sub> and <sup>14</sup>CO<sub>2</sub> measurements: Observation  
594 System Simulations. Atmospheric Chemistry and Physics, 16(9):5665–5683, 2016. ISSN  
595 16807324. doi: 10.5194/acp-16-5665-2016.  
596
- 597 Tom Boden, Bob Andres, and Gregg Marland. Ranking of the world’s countries by 2013 total  
598 CO<sub>2</sub> emissions from fossil fuel burning, cement production, and gas flaring. Technical  
599 report, 2016. URL: [cdiac.ornl.gov/trends/emis/top2013.tot](http://cdiac.ornl.gov/trends/emis/top2013.tot).  
600
- 601 J. Brioude, W. M. Angevine, R. Ahmadov, S. W. Kim, S. Evan, S. a. McKeen, E. Y. Hsie, G. J.  
602 Frost, J. a. Neuman, I. B. Pollack, J. Peischl, T. B. Ryerson, J. Holloway, S. S. Brown, J. B.  
603 Nowak, J. M. Roberts, S. C. Wofsy, G. W. Santoni, T. Oda, and M. Trainer. Top-down  
604 estimate of surface flux in the Los Angeles Basin using a mesoscale inverse modeling



605 technique: Assessing anthropogenic emissions of CO, NO<sub>x</sub> and CO<sub>2</sub> and their impacts.  
606 Atmospheric Chemistry and Physics, 13(7):3661–3677, 2013.  
607  
608 CARB, 2017. California Greenhouse Gas Emission Inventory - 2017 Edition, California Air  
609 Resources Board. Available at <http://www.arb.ca.gov/cc/inventory/data/data.htm>  
610  
611 EDGAR. EDGAR Greenhouse Gas Emissions Inventory v4.2 FT2010, 2011. URL  
612 <http://edgar.jrc.ec.europa.eu/index.php>.  
613  
614 Marc L. Fischer, Nicholas Parazoo, Kieran Brophy, Xinguang Cui, Seongeun Jeong, Junjie Liu,  
615 Ralph Keeling, Thomas E. Taylor, Kevin Gurney, Tomohiro Oda, and Heather Graven.  
616 Simulating estimation of California fossil fuel and biosphere carbon dioxide exchanges  
617 combining in situ tower and satellite column observations. Journal of Geophysical Research:  
618 Atmospheres, 122(6):3653–3671, 2017. ISSN 21698996. doi: 10.1002/2016JD025617.  
619  
620 Mathias Göckede, Anna M. Michalak, Dean Vickers, David P. Turner, and Beverly E. Law.  
621 Atmospheric inverse modeling to constrain regional-scale CO<sub>2</sub> budgets at high spatial and  
622 temporal resolution. Journal of Geophysical Research: Atmospheres, 115(15), 2010.  
623 Graven, H, ML Fischer, T Lueker, S Jeong, TP Guilderson, RF Keeling, R Bambha, K Brophy,  
624 W Callahan, X Cui, C Frankenberg, KR Gurney, BW LaFranchi, SJ Lehman, H Michelsen,  
625 JB Miller, S Newman, W Paplawsky, NC Parazoo, C Sloop, SJ Walker, 2018. Assessment of  
626 Fossil Fuel CO<sub>2</sub> Emissions in California Using Atmospheric Observations and Models,  
627 *Environmental Research Letters*, in review.



628

629 Heather D Graven, Thomas P Guilderson, Ralph, and F Keeling. METHODS FOR  
630 HIGHPRECISION 14 C AMS MEASUREMENT OF ATMOSPHERIC CO 2 AT LLNL.  
631 RADIOCARBON, 49(2):349–356, 2007.

632

633 Heather D. Graven, Thomas P. Guilderson, and Ralph F. Keeling. Observations of radiocarbon  
634 in CO<sub>2</sub> at seven global sampling sites in the Scripps flask network: Analysis of spatial  
635 gradients and seasonal cycles. *Journal of Geophysical Research Atmospheres*, 117(2):n/a–  
636 n/a, January 2012. ISSN 01480227. doi: 10.1029/2011JD016535. URL  
637 <http://doi.wiley.com/10.1029/2011JD016535>.

638

639 Kevin R. Gurney, Daniel L. Mendoza, Yuyu Zhou, Marc L. Fischer, Chris C. Miller, Sarath  
640 Geethakumar, and Stephane De La Rue Du Can. High resolution fossil fuel combustion CO<sub>2</sub>  
641 emission fluxes for the United States. *Environmental Science and Technology*, 43(14):5535–  
642 5541, 2009. 14

643

644 Kevin Robert Gurney, Rachel M. Law, a. Scott Denning, Peter J. Rayner, David Baker, Philippe  
645 Bousquet, Lori Bruhwiler, Yu Han Chen, Philippe Ciais, Songmiao Fan, Inez Y. Fung,  
646 Manuel Gloor, Martin Heimann, Kaz Higuchi, Jasmin John, Eva Kowalczyk, Takashi Maki,  
647 Shamil Maksyutov, Philippe Peylin, Michael Prather, Bernard C. Pak, Jorge Sarmiento,  
648 Shoichi Taguchi, Taro Takahashi, and Chiu Wai Yuen. TransCom 3 CO<sub>2</sub> inversion  
649 intercomparison: 1. Annual mean control results and sensitivity to transport and prior flux  
650 information. *Tellus, Series B: Chemical and Physical Meteorology*, 55(2): 555–579, 2003.



651

652 Susannah Hogue, Eric Marland, Robert J Andres, Gregg Marland, and Dawn Woodard.

653 Uncertainty in gridded CO<sub>2</sub> emissions estimates. *Earth's Future*, pages 1–15, 2016. ISSN

654 23284277. doi: 10.1002/2015EF000343. URL <http://doi.wiley.com/10.1002/2015EF000343>.

655 IPCC. Climate Change 2014: Synthesis Report. Contribution of Working Groups I, II and II

656 to the Fifth Assessment Report of the Intergovernmental Panel on Climate Change. [Core

657 Writing Team, R.K. Pachauri and L.A. Meyer (eds.)]. Technical report, 2014.

658

659 Daniel J Jacob. LECTURES ON INVERSE MODELING. 2007.

660

661 Seongeun Jeong, Ying Kuang Hsu, Arlyn E. Andrews, Laura Bianco, Patrick Vaca, James M.

662 Wilczak, and Marc L. Fischer. A multitower measurement network estimate of California's

663 methane emissions. *Journal of Geophysical Research Atmospheres*, 118(19):11339–11351,

664 October 2013. ISSN 21698996. doi: 10.1002/jgrd.50854. URL

665 <http://doi.wiley.com/10.1002/jgrd.50854>.

666

667 Charles D Keeling, Stephen C Piper, Robert B Bacastow, Martin Wahlen, Timothy P Whorf,

668 Martin Heimann, and Harro A Meijer. Atmospheric CO<sub>2</sub> and <sup>13</sup>CO<sub>2</sub> Exchange with the

669 Terrestrial Biosphere and Oceans from 1978 to 2000: Observations and Carbon Cycle

670 Implications. *A History of Atmospheric CO<sub>2</sub> and Its Effects on Plants, Animals, and*

671 *Ecosystems*, 177:83–113, 2005. doi: 10.1007/b138533. URL

672 <http://www.springerlink.com/index/10.1007/b138533>.

673



- 674 Ingeborg Levin. A novel approach for independent budgeting of fossil fuel CO<sub>2</sub> over Europe by  
675 14CO<sub>2</sub> observations. *Geophysical Research Letters*, 30(23):49–60, 2003. J. C. Lin. A near-  
676 field tool for simulating the upstream influence of atmospheric observations: The Stochastic  
677 Time-Inverted Lagrangian Transport (STILT) model. *Journal of Geophysical Research*, 108  
678 (D16):ACH 2–1–ACH 2–17, 2003.
- 679
- 680 A. J. Manning, S. O’Doherty, A. R. Jones, P. G. Simmonds, and R. G. Derwent. Estimating UK  
681 methane and nitrous oxide emissions from 1990 to 2007 using an inversion modeling  
682 approach. *Journal of Geophysical Research: Atmospheres*, 116(2):1–19, 2011.
- 683
- 684 Thomas Nehrkorn, Janusz Eluszkiewicz, Steven C. Wofsy, John C. Lin, Christoph Gerbig  
685 Marcos Longo, and Saulo Freitas. Coupled weather research and forecasting-stochastic time-  
686 inverted lagrangian transport (WRF-STILT) model. *Meteorology and Atmospheric Physics*,  
687 107(1):51–64, 2010. ISSN 01777971. doi: 10.1007/s00703-010-0068-x.
- 688
- 689 S. Newman, S. Jeong, M. L. Fischer, X. Xu, C. L. Haman, B. Lefer, S. Alvarez, B.  
690 Rappenglueck, E. A. Kort, A. E. Andrews, J. Peischl, K. R. Gurney, C. E. Miller, and Y. L.  
691 Yung. Diurnal tracking of anthropogenic CO<sub>2</sub> emissions in the Los Angeles basin megacity  
692 during spring 2010. *Atmospheric Chemistry and Physics*, 13(8):4359–4372, 2013. ISSN  
693 16807324. doi: 10.5194/acp-13-4359-2013.
- 694 T Oda and S Maksyutov. A very high-resolution (1km<sup>2</sup>×1 km) global fossil fuel CO<sub>2</sub> emission  
695 inventory derived using a point source database and satellite observations of nighttime lights.  
696 *Atmospheric Chemistry and Physics*, 11(2):543–556, 2011



697

698 P. Peylin, S. Houweling, M. C. Krol, U. Karstens, C. Rödenbeck, C. Geels, A. Vermeulen, B.

699 Badawy, C. Aulagnier, T. Pregar, F. Delage, G. Pieterse, P. Ciais, and M. Heimann.

700 Importance of fossil fuel emission uncertainties over Europe for CO<sub>2</sub> modeling: Model

701 intercomparison. *Atmospheric Chemistry and Physics*, 11(13):6607–6622, 2011.

702

703 Peylin P, Law RM, Gurney KR, Chevallier F, Jacobson AR, Maki T, Niwa Y, Patra PK, Peters

704 W, Rayner PJ, Rödenbeck C. Global atmospheric carbon budget: results from an ensemble of

705 atmospheric CO<sub>2</sub> inversions. *Biogeosciences*. 2013 Oct 24;10:6699-720.

706

707 Clive D Rodgers. *Inverse Methods for Atmospheric Sounding*. WORLD SCIENTIFIC, July

708 2000. ISBN 978-981-02-2740-1. doi: 10.1142/3171. URL

709 <http://www.worldscientific.com/worldscibooks/10.1142/3171>.

710

711 J. C. Turnbull, A. Karion, M. L. Fischer, I. Faloona, T. Guilderson, S. J. Lehman, B. R. Miller, J.

712 B. Miller, S. Montzka, T. Sherwood, S. Saripalli, C. Sweeney, and P. P. Tans. Assessment of

713 fossil fuel carbon dioxide and other anthropogenic trace gas emissions from airborne

714 measurements over Sacramento, California in spring 2009. *Atmospheric Chemistry and*

715 *Physics*, 11(2):705–721, 2011.

716

717 C. E. Yver, H. D. Graven, D. D. Lucas, P. J. Cameron-Smith, R. F. Keeling, and R. F. Weiss.

718 Evaluating transport in the WRF model along the California coast. *Atmospheric Chemistry*

719 *and Physics*, 13(4): 1837–1852, February 2013.





720

721 Nassar, R., Sioris, C. E., Jones, D. B. A., and McConnell, J. C.: Satellite observations of CO<sub>2</sub>  
722 from a highly elliptical orbit for studies of the Arctic and boreal carbon cycle, *J. Geophys.*  
723 *Res.- Atmos.*, 119, 2654–2673, doi:10.1002/2013JD020337, 2014.

724

725 Nassar R, Napier-Linton L, Gurney KR, Andres RJ, Oda T, Vogel FR, Deng F. Improving the  
726 temporal and spatial distribution of CO<sub>2</sub> emissions from global fossil fuel emission data sets.  
727 *Journal of Geophysical Research: Atmospheres*. 2013 Jan 16;118(2):917-33.

728

729 Hungershofer, K., Breon, F.-M., Peylin, P., Chevallier, F., Rayner, P., Klonecki, A., Houweling,  
730 S., and Marshall, J.: Evaluation of various observing systems for the global monitoring of  
731 CO<sub>2</sub> surface fluxes, *Atmos. Chem. Phys.*, 10, 10503–10520, doi:10.5194/acp-10-10503-  
732 2010, 2010.

733

734 Chevallier, F., Maksyutov, S., Bousquet, P., Bréon, F.-M., Saito, R., Yoshida, Y., and Yokota,  
735 T.: On the accuracy of the CO<sub>2</sub> surface fluxes to be estimated from the GOSAT  
736 observations, *Geophys. Res. Lett.*, 36, L19807, doi:10.1029/2009GL040108, 2009.

737 Gerbig, C., Lin, J.C., Wofsy, S.C., Daube, B.C., Andrews, A.E., Stephens, B.B., Bakwin, P.S.  
738 and Grainger, C.A., 2003. Toward constraining regional-scale fluxes of CO<sub>2</sub> with  
739 atmospheric observations over a continent: 2. Analysis of COBRA data using a receptor-  
740 oriented framework. *Journal of Geophysical Research: Atmospheres*, 108(D24).

741



- 742 Marland G, Brenkert A, Olivier J. CO<sub>2</sub> from fossil fuel burning: a comparison of ORNL and  
743 EDGAR estimates of national emissions. *Environmental Science & Policy*. 1999 Jun  
744 1;2(3):265-73.  
745
- 746 Grell GA, Dudhia J, Stauffer DR. A description of the fifth-generation Penn State/NCAR  
747 mesoscale model (MM5).  
748
- 749 Nakanishi M, Niino H. An improved Mellor–Yamada level-3 model with condensation physics:  
750 Its design and verification. *Boundary-Layer Meteorology*. 2004 Jul 1;112(1):1-31.  
751
- 752 Nakanishi M, Niino H. An improved Mellor–Yamada level-3 model: Its numerical stability and  
753 application to a regional prediction of advection fog. *Boundary-Layer Meteorology*. 2006  
754 May 1;119(2):397-407.  
755
- 756 Hong SY, Noh Y, Dudhia J. A new vertical diffusion package with an explicit treatment of  
757 entrainment processes. *Monthly weather review*. 2006 Sep;134(9):2318-41.  
758
- 759 Feng S, Lauvaux T, Newman S, Rao P, Ahmadov R, Deng A, Díaz-Isaac LI, Duren RM, Fischer  
760 ML, Gerbig C, Gurney KR. Los Angeles megacity: a high-resolution land–atmosphere  
761 modelling system for urban CO<sub>2</sub> emissions. *Atmospheric Chemistry and Physics*. 2016 Jul  
762 22;16(14):9019-45.  
763



- 764 Turnbull JC, Sweeney C, Karion A, Newberger T, Lehman SJ, Tans PP, Davis KJ, Lauvaux T,  
765 Miles NL, Richardson SJ, Cambaliza MO. Toward quantification and source sector  
766 identification of fossil fuel CO<sub>2</sub> emissions from an urban area: Results from the INFLUX  
767 experiment. *Journal of Geophysical Research: Atmospheres*. 2015 Jan 16;120(1):292-312.  
768
- 769 Seibert P, Beyrich F, Gryning SE, Joffre S, Rasmussen A, Tercier P. Review and  
770 intercomparison of operational methods for the determination of the mixing height.  
771 *Atmospheric environment*. 2000 Jan 1;34(7):1001-27.  
772
- 773 Jones A., Thomson D., Hort M., Devenish B. (2007) The U.K. Met Office's Next-Generation  
774 Atmospheric Dispersion Model, NAME III. In: Borrego C., Norman AL. (eds) *Air Pollution  
775 Modeling and Its Application XVII*. Springer, Boston, MA  
776
- 777 Chen, F., and J. Dudhia (2001), Coupling an advanced land surface hydrology model with the  
778 Penn State NCAR MM5 modeling system. Part 1: Model implementation and sensitivity,  
779 *Mon. Weather Rev.*, 129, 569–585.



Air Basin	Name	Code	Vulcan (TgC/yr)	EDGAR (TgC/yr)	SD Prior Unc. 1- $\sigma$ (%)	Vulcan - EDGAR (TgC/yr)
1	North Coast	1.NC	1.0	1.6	59	-0.6
2	Northeast Plateau	2.NP	0.4	1.3	96	-1.0
3	Sacramento Valley	3.SV	6.8	7.4	8	-0.7
4	Mountain Counties	4.MC	2.2	2.0	51	0.1
5	Lake County	5.LC	0.1	0.2	65	-0.2
6	Lake Tahoe	6.LT	0.1	0.1	42	0
7	Great Basin Valleys	7.GBV	0.2	0.6	100	-0.4
8	San Joaquin Valley	8.SJV	8.6	20.2	35	-11.6
9	North Central Coast	9.NCC	6.0	2.2	71	3.8
10	Mojave Desert	10.MD	6.1	4.3	17	1.8
11	South Central Coast	11.SCC	4.4	3.4	21	1.0
12	Salton Sea	12.SS	1.4	1.7	55	-0.3
13	San Francisco Bay	13.SFB	16.4	17.5	22	-1.2
14	South Coast	14.SC	26.9	35.5	12	-8.6
15	San Diego	15.SD	6.6	6.5	10	0.1
<b>Total California</b>			<b>89.6</b>	<b>104.7</b>	<b>8</b>	<b>-17.8</b>

Table 1: The 15 air basins of California with respective emissions as estimated by Vulcan and EDGAR. Also shown are the SD prior uncertainty estimate (Fischer et al., 2017), and difference in magnitude between Vulcan and EDGAR for each air basin. Air basin numbers correspond to those marked in Figure 1.

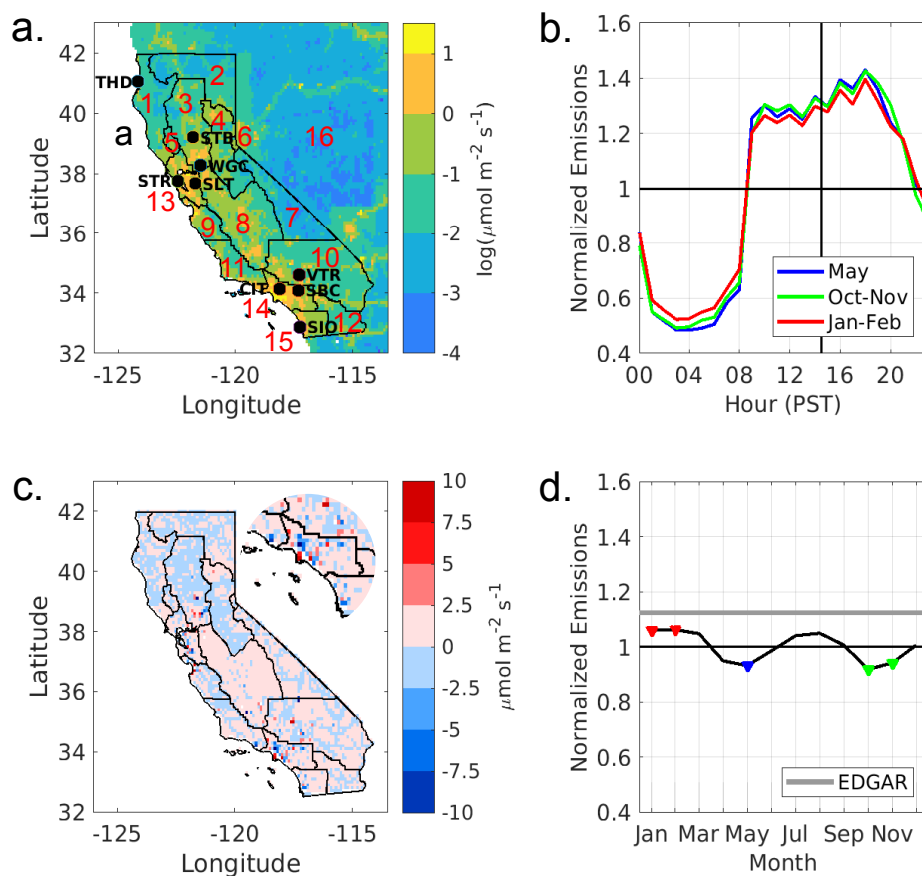


Figure 1: **a.** The location of the 9 tower sites in the observation network (marked with black circles): Trinidad Head (THD), Sutter Buttes (STB), Walnut Grove (WGC), Sutro (STR), Sandia-Livermore (LVR), Victorville (VTR), San Bernardino (SBC), Caltech (CIT) and Scripps Institute of Oceanography (SIO). The 15 air basins are marked out with black lines with region 16 representing emission from outside California within the model domain. Underlaid is a map of annual mean  $f\text{CO}_2$  emissions from the Vulcan v2.2 emission map within the United States and EDGAR v4.2 (FT2010) for emission from outside the U.S. **b.** Vulcan diurnal emissions normalized to campaign averaged emissions for the 3 campaigns, **c.** Scaled EDGAR subtracted from Vulcan emissions map, where EDGAR has been scaled to have the same air basin total emissions. The inset shows an enlarged view of southwestern California. **d.** Average monthly emissions normalized to Vulcan annual emissions. Shown in both **b** and **d** is EDGAR annual invariant emissions (grey).



Transport Model	Meteorology	Domain	Model Resolution			References
			Horizontal	Vertical (nLevels / Max Height)	Temporal	
WS-LBL	WRF (v3.5.1)	North America	1km, 4km, 12 km, 36km	50 / 16 km	1 hour	(Lin, 2003; Nehr Korn et al., 2010);
WS-CTL	WRF (v2.1.2)	North America	0.1°, 1°	29 / 25 km	1 hour	(Carbon Tracker, 2017)
UM-NAME	Unified Model	Global	17km, 25km	59 / 29 km	3 hours	(Ryall et al., 1998)

Table 2: Comparison of the three atmospheric transport models used in this study.

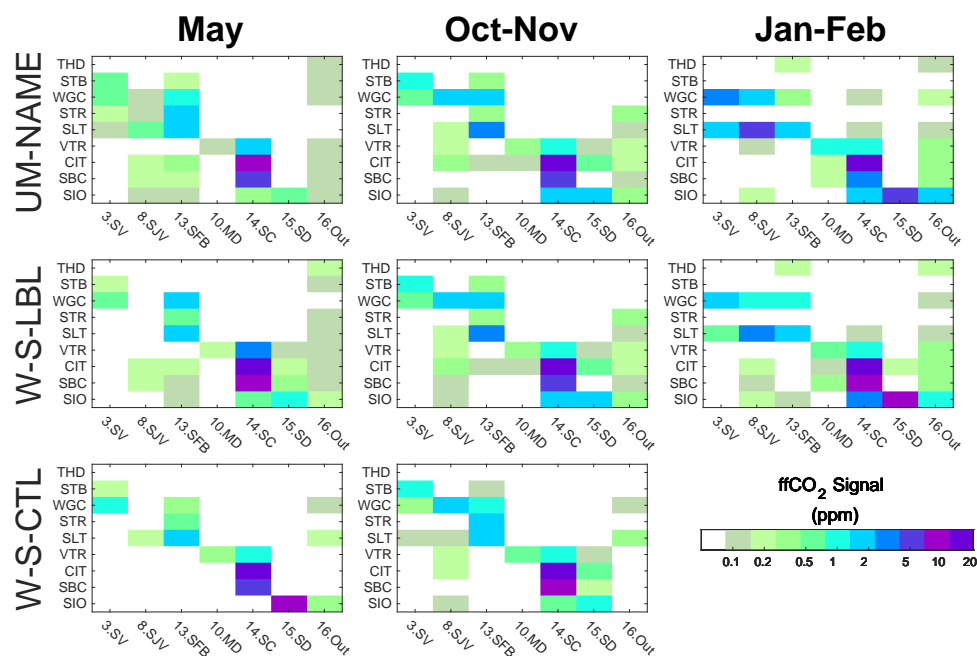


Figure 2: The average  $ffCO_2$  signal (ppm) simulated by each atmospheric transport model as a result of emissions from the 6 largest emitting air basins and one outside California region at each observation site over the three measurement campaigns. Signals were simulated based on the EDGAR emission map.

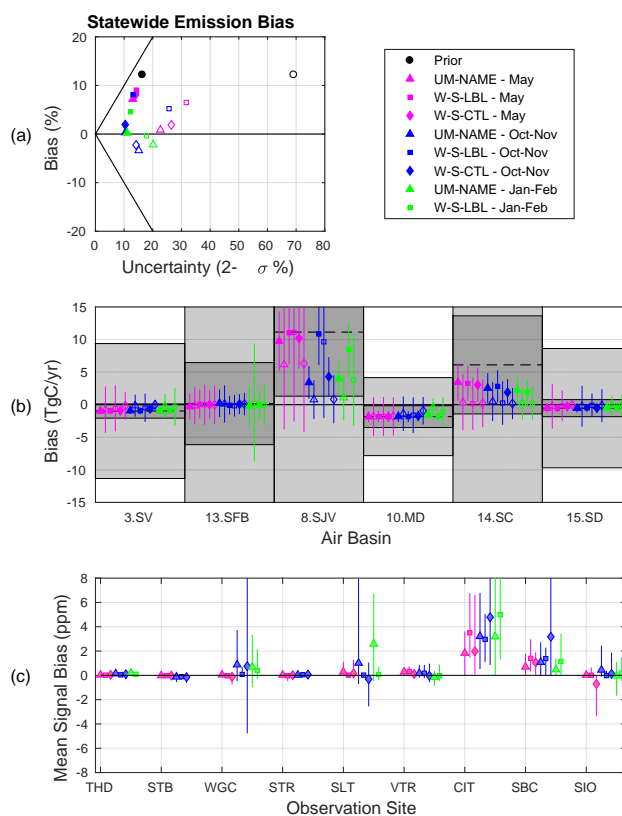


Figure 3: (a) Statewide and (b) individual air basin inversion results for an error in the magnitude of prior emissions. Prior emissions are given by EDGAR and true emissions are given by EDGAR scaled to Vulcan total in each air basin. Air basin results are shown for Sacramento Valley (3.SV), San Francisco Bay (13.SFB), San Joaquin Valley (8.SJV), Mojave Desert (10.MD), South Coast (14.SC) and San Diego (15.SD). Prior results are presented by black markers and posterior results are represented by colored markers. Filled markers show results using SD prior uncertainty and empty markers show results using 70% prior uncertainty. The prior bias in each air basin is given by the dashed lines in (b) with SD prior uncertainty (dark grey) and 70% prior uncertainty (light grey). Prior and posterior uncertainties are expressed as  $2\text{-}\sigma$ . The bottom plot (c) shows the mean signal error in simulated average  $\text{ffCO}_2$  concentration. Mean signal error is calculated by subtracting the average true signal from the average prior signal. Error lines are drawn between the maximum and minimum signal bias per campaign.



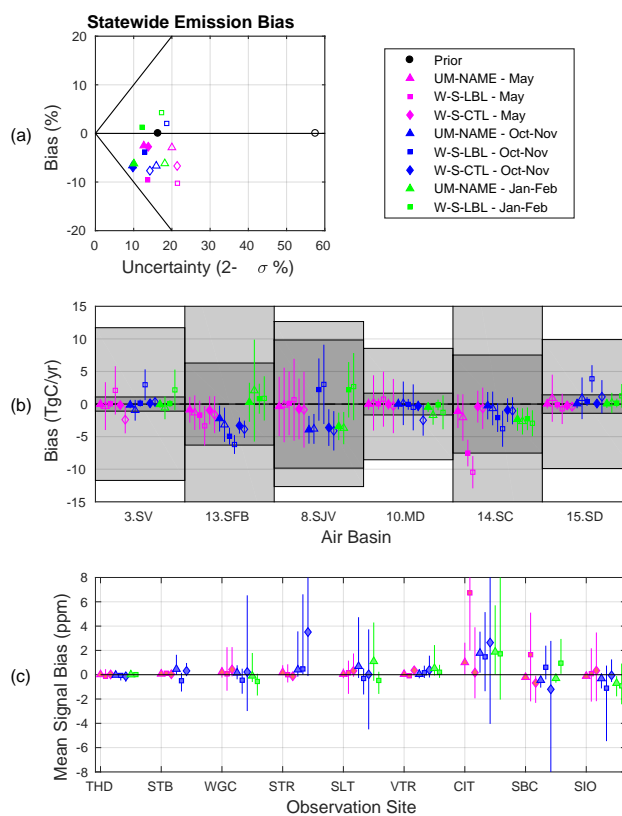


Figure 4: (a) Statewide and (b) individual air basin inversion results for an error in the spatial distribution of prior emissions. Prior emissions are given by EDGAR scaled to Vulcan emissions totals in each air basin and true emissions are given by Vulcan. The bottom plot (c) shows the mean signal error in simulated average  $\text{ffCO}_2$  concentration.

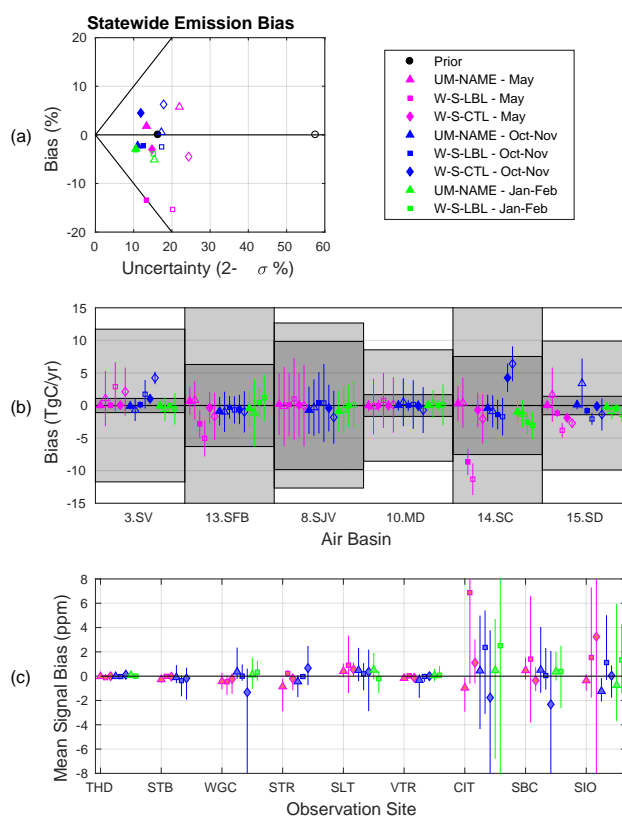


Figure 5: (a) Statewide and (b) individual air basin inversion results for an error in the temporal distribution of prior emissions. Prior emissions are given by temporally varying Vulcan and true emissions are given by annually averaged Vulcan. Prior emissions were scaled to be the equal in magnitude to annually averaged Vulcan emissions. The bottom plot (c) shows the mean signal error in simulated average  $\text{ffCO}_2$  concentration.

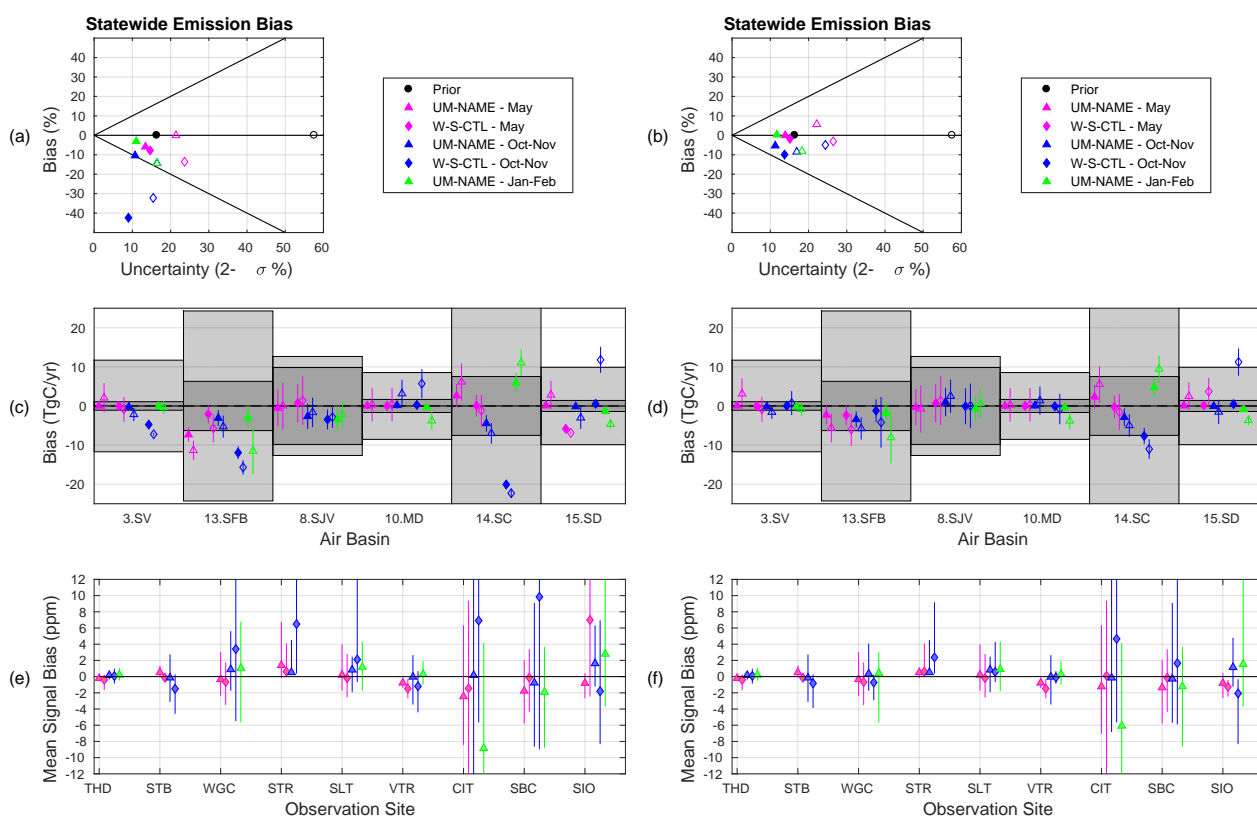


Figure 6: Inversion results for the experiment where the atmospheric transport in the prior simulation uses WS-CTL or UM-NAME but the atmospheric transport in the true simulation uses WS-LBL. Posterior statewide emissions (a, b), individual air basin emissions (c, d), and percentage error in simulated average  $f\text{CO}_2$  concentration (e, f) are shown with no outlier removal (first column) and outliers removed (second column). Prior and true emissions are given by annually averaged Vulcan.

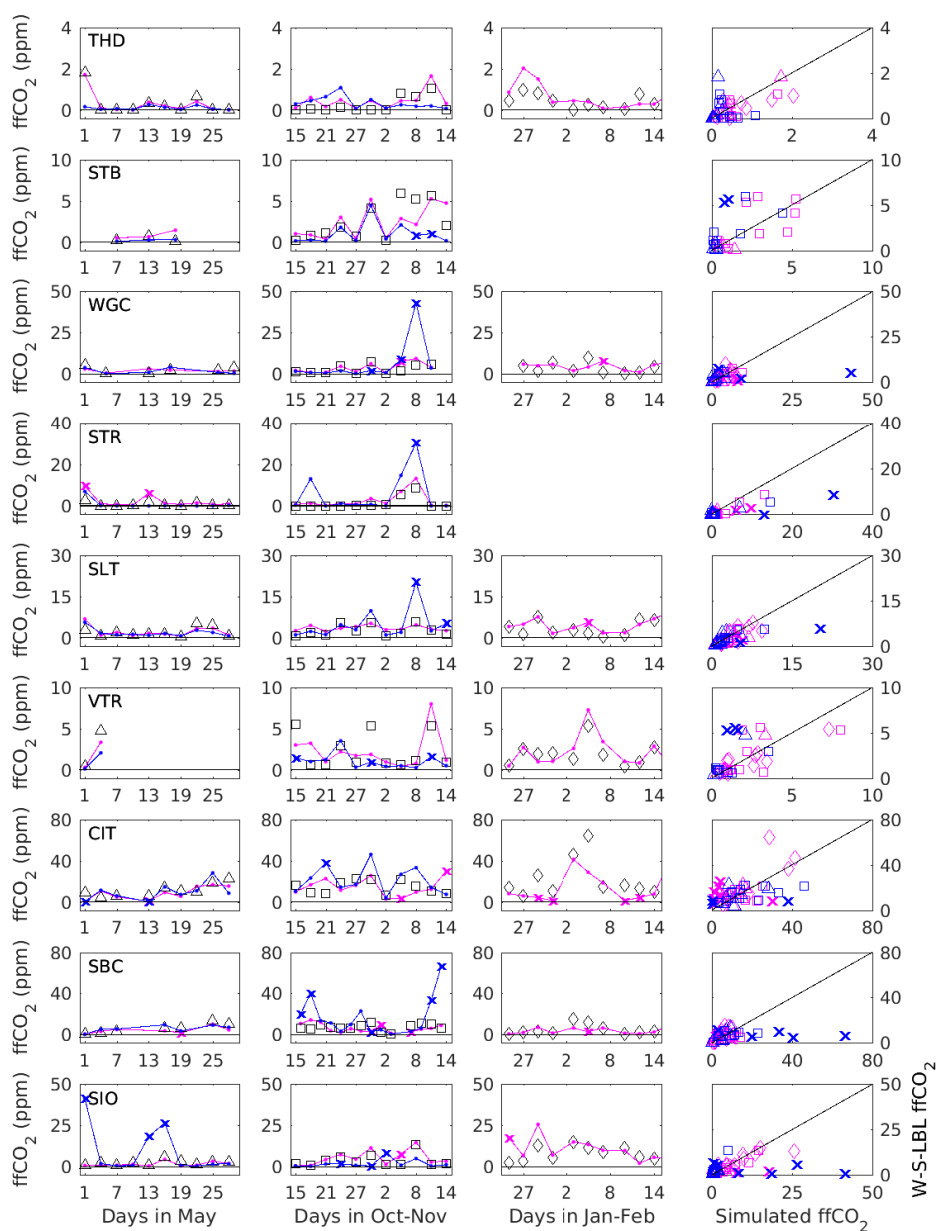


Figure 7: All simulated  $\text{fCO}_2$  from May (first column), October-November (second column), and January-February (third column). Simulated  $\text{fCO}_2$  using W-S-LBL are shown in black markers (triangles for May, squares for Oct-Nov and diamonds for Jan-Feb) whilst prior W-S-CTL signals are shown in blue and UM-NAME signals in magenta. All simulated signals are generated using the Vulcan gridded emissions map. The fourth column shows true vs prior  $\text{fCO}_2$  signals, with colors corresponding to models and markers corresponding to campaigns. Outliers omitted from the standard inversion are shown by an x.